Università degli Studi di Padova

Padua Research Archive - Institutional Repository

Enhancing the efficiency of kW-class vanadium redox flow batteries by flow factor modulation: An experimental method

(Article begins on next page)

Enhancing the Efficiency of kW-class Vanadium Redox Flow Batteries by Flow Factor Modulation: An Experimental Method

Massimo Guarnieri, Andrea Trovò and Francesco Picano

Department of Industrial Engineering, University of Padua, Padova, Italy

Interdepartmental Centre Giorgio Levi Cases for Energy Economics and Technology, University of Padua, Padova, Italy

Abstract

The paper presents a control method of the electrolyte flow factor in kW-class Vanadium Redox Flow Batteries that minimizes transport losses without affecting the battery's electrical performance. This method uses experimental data acquired on a 9 kW/27kWh test facility at varying operating conditions. The effects of overpotentials on the polarization curves are then modeled as nonlinear electrical resistances that vary with the stack current, state of charge and electrolyte flow rates. Our analysis of these variables shows that the optimal performance is found if the flow factor is modulated during operation according to stack current and the battery state, so as to minimize the overall flow-dependent losses. The optimal profiles have been identified as functions of the battery's operating conditions. Based on these results, a dynamic control for the electrolyte flow rates has been implemented at a software level (i.e. without modifying the hardware of the test facility), which is capable of maximizing the round-trip efficiency and exceeds the performance achieved with a constant flow factor strategy, as proposed in previous literature. The implementation of the optimal flow rate control requires a preliminary test campaign to collect performance data, which are then used in the control protocol to manage the battery's operation. This scheme is easily implementable at a software level in other industrial redox flow batteries.

Keywords: Vanadium Redox Flow Battery, transport losses, flow rate control, round-trip efficiency, performance optimization.
`elsarticle.cls`, LaTeX, Elsevier, template
2010 MSC: 00-01, 99-00

★Fully documented templates are available in the elsarticle package on CTAN.
Email address: `massimo.guarnieri@unipd.it` (Massimo Guarnieri, Andrea Trovò and Francesco Picano)

1. Introduction

Vanadium Redox Flow Batteries (VRFBs) are increasingly attracting attention thanks to their intrinsic advantages, such as independent sizing of power and energy, long cycle life and good energy efficiency [1]. VRFBs are particularly competitive for long discharges (namely at high energy-to-power ratios) and also for long storage times (such as in seasonal storage), while being capable of virtually no self-discharge. Although VRFBs present lower energy efficiency than Li-ion batteries, they are more competitive in terms of life cycle assessment (i.e. environmental impact) because Vanadium is completely recyclable, in contrast to Lithium [2]. As regards large plants, due to their structure, VRFBs are better fitted than Li-ion batteries, which involves a very large number of cells, with a consequently higher fault risk. At present, the largest electrochemical storage plant is the 200 MW 800 MWh VRFB plant under construction by Rongke Power. In addition, VRFBs are suitable for a wide range of services in smart grids, both fast (i.e. power quality, such as frequency regulation and peak shaving) and slow (i.e. energy management, such as load leveling and investment deferral) [3]. These features entitle the VRFB technology to be a major candidate in the future energy storage scenarios and to be capable of widespread commercialization [4]. Extensive research has been carried out in the development of advanced materials and significant results have been achieved in the last years. Recent improvements on the electrolytes have led to higher energy densities as reported by Choi et al. [5] and by Roe et al. [6], who employed a 3 M vanadium electrolyte. Concerning electrodes, Di Blasi et al. [7] investigated the charge/discharge performance of a carbon fiber-based electrode in a short stack, and an experimental comparison of the electrochemical energy conversion performance of a single-cell VRFB with different flow fields was performed by Kumar et al. [8]. In addition, Greco et al. [9] and Banerjee et al. [10] studied the effects of the electrode micro-structure on the overall electrochemical performance. The undesired crossover of vanadium ions and water through the ion-exchange membrane and consequent capacity loss have been investigated by Sun et al. [11] with the aim to obtain a trade-off between high ionic conductivity and decreased crossover membranes; similar studies were reported by Lei et al. [12] and Ashraf et al. [13]. The electrolyte transport effects on the battery performance are also receiving increasing attention [14]. In this framework, the effect of different cell structure designs was studied by several groups, e.g. Darling et al. [15], Ke et al. [16] and Zheng et al. [17]. In addition, Arenas et al. [18, 19] and Xu et al. [20] demonstrated that the battery's performance strongly depend on the control of the process variables. Watt-Smith et al. [21] and Pugach et al. [22] achieved similar results in the case of large-scale VRFB systems. The charging procedure is also responsible for the battery performance, nevertheless it is often borrowed from other batteries, with an operation that consists in charging the battery under constant current (galvanostatic mode) until the voltage reaches a given value and then in switching to constant voltage (potentiostatic mode) to complete the charge [23]. In VRFBs, this charging mode as been claimed to be convenient to prevent hydrogen and oxygen evolution [24].

Although this charge profile is convenient in testing cells in a laboratory and in charging portable electronics and electric cars, it is little applicable to industrial size batteries operating in grids to compensate the mismatch between the power generated by intermittent renewable sources and load demand as reported by Guarnieri et al. [25, 26]. In VRFBs operating at variable charge/discharge currents, the electrolyte flow rate control assumes a pivotal importance at the aim of optimizing the battery performance because high flow rates improve the cell performance by reducing overpotentials but increase the hydraulic losses and pumping power demand [27].

To address this problem, techniques based on numerical algorithms have been investigated at an analytical level, such as the fuzzy logic controller [28], and the gain scheduling control [29]. These methods follow synthetic schemes, which fail to take into account all of the real physical variables of the battery.

Some studies have examined the pressure drops and pumping power demand under varying electrolyte flow rates in different cell architectures, aiming to achieve an optimal electrolyte flow bed in the electrodes [30]. To maximize the battery efficiency, Yang et al. [31] have analyzed the cell performance while keeping the flow rate constant during operation and only varying the current density depending on the state of charge (SOC).

Xu et al. [32] developed an analysis of the effect of the SOC-dependent electrolyte viscosity on the battery's performance, but they did not proposed a consequent control strategy.

Ling et al. [33] studied the effect of a pulsating electrolyte flow rate in a single cell VRFB, showing that a short flow period followed by a long flow termination can reduce the pumping power demand by more than 50%.

Ma et al. [34] experimented on an electrolyte flow rate control in a 1 kW-scale VRFB that improved the battery efficiency simply by stepping up the flow rate at the end of charge and discharge to compensate for low reactant concentration. They showed that this strategy can increase the system efficiency by 8% compared to a constant flow rate, showing the advantage of a variable flow rate.

Fu et al. [35] proposed a numerical analysis of a VRFB for investigating the effect of the flow rate on the battery efficiency by taking into account the concentration overpotentials and the related pumping power. They proposed a framework for determining the optimal flow rate under varying operating conditions, which can increase the stack efficiency by 3%.

Recently, Xiao and Tan [36] proposed a numerical method for increasing the efficiency of a complete VRFB system by varying the flow rate within a given range, such that the pump efficiency maintains high values. Their simulations indicate an increase of 3.34% and 3.84%, respectively, showing the superior profitability of a variable flow rate control. However, their analysis is improperly based on the pump efficiency curve at constant speed for different hydraulic circuits instead of that at variable speed for the same hydraulic circuit, which has compromised the validity of their results.

Tang et al. [37] have numerically computed the transport losses in a 40-cell stack as a function of the flow factor, namely the ratio of flux of electric

charges (ions) provided by electrolyte flow for electrochemical reactions and the generated electric current, which is always higher than one to ensure effective reactions. They investigated the battery's performance with a constant flow factor, finding that a value of 7.5 provides the highest system efficiency. König et al. [38] developed a numerical investigation of the behavior of a 6-kW VRFB, finding that the efficiency can be improved by varying the flow factor depending on SOC and the battery's current.

Nevertheless, experimental studies on flow rate dynamic control in kW-class VRFB systems depending on the battery performance have yet to be published, to the best of our knowledge.

This paper reports a study on the modulation of the electrolyte flow rate to minimize the battery voltage drop without affecting the converted power and hence to maximize the battery efficiency. This study is based on an experimental investigation that was carried out on a kW-class VRFB test facility. An optimal flow rate dynamic control has been identified for the first time and it has been implemented in the LabVIEW-based battery management system of the VRFB test facility to assess its effectiveness.

This paper is organized as follows. The kW-class test facility used in the measurement campaign and validation tests is presented in Section 2. The measurements of the cell losses are analyzed in Section 3 to correlate them with the electrical behavior of the VRFB. Section 4 reports the procedure for the optimal flow factor identification and presents the performance (namely, the battery's round-trip efficiency) that we obtained with the control algorithm. Validation tests and efficiency assessment are reported in Section 5 and the conclusions are discussed in Section 6.

2. Experimental setup

The Industrial-Scale VRFB (IS-VRFB) test facility (Fig. 1) is in operation at the Energy Storage and Conversion Laboratory of the University of Padua [39]. The stack consists of 40 cells with 30 cm × 20 cm cross-sectional area, and each cell consists of a Nafion$^{®}$ 212 membrane and two 5.7-mm graphite carbon electrode (Beijing Great Wall, China) included between two flat graphite bipolar plates with a flow through electrolyte distribution [40]. The electrolytes consist of vanadium solutes with a concentration of $c_V = 1.6$ mol L^{-1} in 4.5 mol L^{-1} sulfuric acid solution. Two tanks containing 550 L of electrolyte each store an energy of 27 kWh. The tanks are hermetically closed and are maintained in nitrogen atmosphere to prevent vanadium species from atmospheric oxygen contamination.

The battery is provided with two closed hydraulic circuits, including pumps, piping and valves for electrolyte circulation between stack and tanks. The two pumps (PMD-641 by Sanso, Japan) have PVC volutes and impellers, the latter being magnetically driven by three phase electric motors, which are controlled by two inverters (DC1 by Eaton, US). The Power Management System (PMS) that provides the battery charge and discharge consists of a remotely driven bidirectional static converter that can operate in the ranges ± 75 A and $0-85$

Nomenclature

Full names

A	cell cross-section area [cm^2]
c	Vanadium species concentrations [mol L^{-1}]
c_r	felt compression ratio
c_V	Vanadium molar concentration [mol L^{-1}]
F	Faraday constant [96,485 C mol^{-1}]
Fl	flow mater
h_{cr}	felt thickness after compression [mm]
h_0	felt thickness before compression [mm]
I	stack current [A]
In	inverter
K	gas constant [8.314 J mol^{-1} K^{-1}
N	number of cells in the stack
P	power [W]
Pu	pump
Q	electrolyte flow rate [L min^{-1}]
q	specific flow rate [cm s^{-1}]
R	electrical resistance [Ω]
RTE	round trip efficiency
SOC	state of charge
t	time [s]
T	temperature [K]
V	voltage [V]
Va	sensorized valves
V_0	open circuit voltage (OCV) [V]
z	number of electron transfer

Subscripts

a	activation
b	bipolar plate
ch	charge
dh	discharge
e	electrode
el	electrolyte
w	gross hydraulic
i	internal
k	key
m	membrane
o	ohmic
opt	optimal
Q	flow rate dependent
st	stack
t	transport
$+$	positive electrolyte
$-$	negative electrolyte

Greek Symbol

α	flow factor
Δp	pressure drop [Pa]
Δr	index of the incidence of $R_a + R_t$ [%]
ϵ	porosity after compression
ϵ_0	porosity before compression
σ_f^{eff}	effective carbon felt conductivity [S m^{-1}]
σ_{el}^{eff}	effective electrolyte conductivity [S m^{-1}]
σ_s	conductivity of the solid carbon felt material [S m^{-1}]

V in either voltage or current controlled mode (potentiostatic or galvanostatic mode; Dana, Italy). A passive load made with six variable resistors allows discharges at higher currents (up to 600 A). The facility's instrumentation provides the following measurements: stack current and voltage, cell voltages, open circuit voltage (by means of a small OCV cell), electrolyte flow rates, electrolyte differential pressures at stack inlets and outlets, electrolyte temperatures at the stack inlets and outlets, electrolyte level in the tanks, and room temperature. A wattmeter measures the power fed from the grid to the hydraulic circuits.

The Battery Management System (BMS) that supervises the facility is an in-house system that is built around a PC with LabVIEW software, a National Instruments (NI, US) compact DAC interface, a system of optoisolators (Isoblock by Verivolt, US), insulation measurement transformers, and a Programmable Logic Controller (PLC). It has been designed to provide adaptable high level Supervisory Control And Data Acquisition (SCADA) functions. Notably, it ensures a precise flow rate control of each pump through a proportional-integrative-derivative (PID) controller (Fig.1), in which an analog voltage $(0-10$ V) signal drives the inverter based on a negative feedback logic that uses the measured analog signals $(0-20$ mA) provided by a high performance flow-meter (Proline Promag by Endress+Hauser, Switzerland). This architecture allows us to obtain the desired electrolyte flow rates profiles by means of in-house developed driving algorithms which make use of the experiment measurements, such as current I and SOC.

The test facility has been already operated at currents up to 400 A in fast mode and 350 A in steady state mode (i.e. at 665 mA cm^{-2} and 583 mA cm^{-2}, respectively) with residual cell voltages of 0.55 V and 0.46 V [41]. Peak powers of 9 kW and 8 kW were achieved in the two operating modes, at currents of 320 A and 260 A, respectively.

3. Analysis of cell overpotential losses

The analyses presented hereafter have made use of the measurements taken on IS-VRFB during charge and discharge operations, which were carried out at different stack currents I, state of charges $SOCs$, and electrolyte flow rates Q. In VRFBs, due to species crossover occurring through cell membranes, the volume of the positive electrolyte decreases and the volume of the negative electrolyte increases during the charge phase, and vice versa during the discharge phase. Models of this effect have been recently reported Wei et al. [42, 43]. The net effect in a round-trip cycle is that the volume of the positive electrolyte increases and the volume of the negative electrolyte decreases, as reported in [44]. During the experiments on IS-VRFB, a volume changes of $\simeq$ 4 L (i.e 0.7%) in each charge/discharge cycle was observed. A balancing operation through a bypass pipe interconnecting the two tanks was operated every 10 cycles to compensate for this effect [39].

At the cell level, the polarization curve of an electrochemical device (namely, the voltage as a function of the current density) depends on three overpotentials that are responsible for energy losses [45]. Activation overpotentials appear at

low current density and have typically a minor role in VRFBs, in which the dominating effect in a large range of current density consists of the linear ohmic overpotentials. Concentration overpotentials may prevail at high current density, causing a dramatic voltage drop and the rapid vanishing of voltage at the limiting current densities. At a battery level, similar polarization curves correlate the stack voltage and current. The relative effects of the three overpotentials in a VRFB depend on several parameters, such as current collector and electrodes design, membrane composition and thickness, electrolyte flow rates, and state of charge.

Fig. 2 shows the discharge polarization curves taken on the IS-VRFB in steady-state operating conditions at stack currents up to about 350 A. They have been obtained at SOC ranging between 10% and 90% and at electrolyte flow rates $Q = 10$ L min^{-1} and $Q = 29.5$ L min^{-1} (i.e. at a specific flow rates $q = 6.9 \times 10^{-3}$ cm s^{-1} and $q = 20.8 \times 10^{-3}$ cm s^{-1}, respectively).

Given that the scope of our analysis was to investigate the steady-state performance of the battery expressed by these curves, the dynamic capacitive effects of the electrodes were neglected and only the steady-state adynamic effects related to overpotentials were taken into account. As shown in Fig. 2, in general these polarization curves are non-linear over the whole electric current ranges. For the purposes of the following analysis, the overpotetials were modeled by means of non-linear electrical resistances so that the stack voltage drop ΔV was expressed as:

$$\Delta V = V_0 - V = (R_a + R_o + R_t)\, I = R_i\, I \tag{1}$$

where R_a, R_o and R_t are the activation, ohmic and transport equivalent resistances, respectively, and their sum R_i is the internal stack resistance as reported by Fu et al.[46] and Ontivoros et al. [47]. Although the representation of overpotentials by means of electrical resistances may seem a strong simplification, it was convenient in this study because it allowed a straightforward quantification and comparison of the intrinsically different overpotentials. This approach conforms similar modeling technique used in other VRFB electric performance investigations [48] and is commonplace in modeling electrical devices such as induction motors, negative-resistance amplifiers and active resistors. The resistances R_a, R_o and R_t are functions of I, due to the non-linearity of the $V(I)$ curves, and also of SOC and Q. R_a mainly affects the polarization curve at small I values, R_o in the medium range and R_t at high values, consistently with the aforementioned overpotential features.

Fig. 2 shows that the curves at different Q and at the same SOC present the same open circuit voltage (OCV), i.e. $V_0(SOC)$ at $I = 0$. Fig. 2 also shows that most polarization curves $V(I)$ of IS-VRFB exhibit a linear behavior at low I values, indicating that the activation losses are small compared to the other two terms, as reported in the literature for other VRFB systems by Chen et al. [49], Ressel et al. [50], and Pugach et al. [51], so that we can assume:

$$R_i \approx R_o + R_t \tag{2}$$

In addition, most curves present a sudden voltage drop as I increases and

this drop occurs as sooner as SOC is smaller, in both cases at $Q = 10$ L min^{-1} and $Q = 29.5$ L min^{-1}. In polarization curves at low SOC and low Q, these dramatic voltage decreases present an early occurrence. This behavior is due to transport losses and is represented by a strong increase of the electrical resistance R_t. This indicates how crucial the flow rate control is to pump the optimal amount of electrolyte that ensures proper electrochemical reactions while avoiding wasting pumping power, so that the battery electrical performance are kept at the highest levels (i.e. the internal resistance remains as low as possible). The flow factor α is a useful parameter to correlate electrolyte flow rates and electric performance. As already stated, this is given by the ratio between the flux of charges provided by the electrolyte flow for the reactions and the electric current generate in all the cells. In the charge/discharge phases, it is respectively expressed as:

$$\alpha = \frac{Q\,F\,c_V\,(1 - SOC)}{N\,I} \tag{3}$$

$$\alpha = \frac{Q\,F\,c_V\,SOC}{N\,I} \tag{4}$$

with F the Faraday constant, c_V the Vanadium total concentration and N the number of cells in the stack. Eq. (3) and eq. (4) show that, during an operation fixed Q, α changes because of SOC and I variations. In particular, α depends linearly on I and inversely on Q. The flow factor cannot be smaller than $\alpha = 1$ because in this condition the electrolyte flow rates provide exactly the ions needed to produce the electric current I. Therefore, $\alpha = 1$ would be the ideal condition as regards minimizing the pumping power but it would be very dangerous operating the battery at such α value because it is almost impossible that all reagent ions reach the active sites: $\alpha = 1$ would cause reactions in cell materials other than the electrolytes, resulting in cell malfunction and even battery failure as reported in [52] and [53]. Consequently, α is usually kept at values of $7-8$, to ensure proper electrolyte reactions [37].

3.1. Optimal flow rate identification

To investigate this behavior, a new set of polarization curves $V(I)$ was built by using the measurements of a new experimental campaign carried out at different $SOCs$, in which Q was continuously varied so as to keep α constant while increasing I, exploiting the operational flexibility allowed of the pumps feedback control. In these tests, the BMS controlled the pumps and also the PMS that was operated as a controlled electronic converter both in charge and discharge. This operation mode limited the stack current to the PMS rated current of ± 75 A, but also provided some advantages. In fact, it allowed exploring a conveniently wide range of $SOCs$ in each charge/discharge test, e.g. $SOC = 13\%-87\%$ at 30 A and $SOC = 28\%-72\%$ at 70 A, which would be unaccessible at higher currents, because of limitations deriving from the maximum available flow rates and from the risk of hydrogen evolution [24]. Moreover, the maximum current density achieved of 116 mA cm^{-2} was comparable with the

values obtained in similar analyses reported in the literature [54], [55]. Several α values could be explored (up to nine for each SOC) with the lower and upper limits imposed by the minimum and maximum pump flow rates; that is, $Q = 3$ L min^{-1} and $Q = 29.5$ L min^{-1}.

Fig. 3 shows these polarization curves drawn at constant α for four $SOCs$. Each curve appears linear, resulting in a constant internal resistance R_i, with no dramatic increases at high currents. In addition, the reduction of the slope with increasing α results in a lower and lower R_i. As α increases and approaches a key value α_k, these polarization curves converge to a limit linear profile with a minimal slope, namely with minimal internal resistance $R_k = -\Delta V_k / \Delta I$ and the cell electrical performance cannot be enhanced any further by increasing α.

According to these results, transport losses are important as long as $\alpha < \alpha_k$. Conversely, when α is higher than α_k the ohmic losses are the dominant effect that produces the linear behavior of $V(I)$. Once the concentrations of the reactant ions supplied at the active sites in the porous electrodes exceed the values needed to efficiently sustain the reactions, a further increase of the flow rate can no longer improve the reaction rate. In these conditions, the transport equivalent resistance R_t becomes much smaller than the ohmic equivalent resistance R_o. This latter resistance depends on the cell and electrolyte electric properties but not on the electrolyte flow rate, in such a way that at constant SOC the relationship between voltage and current results linear. Fig. 4 shows that α_k is a weakly increasing function of SOC.

We infer that controlling Q according to each different operating condition (namely, according to SOC and I) to maintain $\alpha \simeq \alpha_k$ constitutes an optimal strategy for maximizing the electrical performance of a VRFB (i.e. for minimizing the hydraulic losses without affecting the power conversion performance).

3.2. Characterization at $\alpha \geq \alpha_k$

Because the convergence profile of all polarization curves at $Q = const$ and $\alpha \geq \alpha_k$ is linear, it is characterized only by its slope; that is, by its key internal resistance, $R_k = \Delta V_k / \Delta I$ that is a function of the SOC only: $R_k(SOC)$. Similarly to the ohmic losses that it represents, the resistance R_o included in eq. 2 depends on the resistive behavior of the bipolar plates, of the electrolyte-soked porous electrodes, of the ion-exchange membrane and of the contacts between these components. Instead, R_o does not depend on α and, consequently, any increase of R_i that occurs when α is smaller than α_k can be attributed to the transport losses represented by R_t. Hence, we can assume that:

$$R_o \simeq R_k \qquad (5)$$

At different SOC, the electrolyte concentrations in the porous electrodes change, causing a variation of the ohmic resistance $R_o = R_o(SOC)$, because the conductivities of the electrolyte species differ. Fig. 4 shows that R_o is a decreasing function of SOC, due to the higher concentration of $V(II)$ and $V(V)$ at higher SOC. To check the consistency of the previous assumptions, R_o was evaluated as due the series of the cell membranes, with total resistance

R_m, of the cell porous felt electrodes, with total resistance R_e, and of the the graphite bipolar plates, with total resistance R_b. The contact resistances were neglected:

$$R_o = R_m + R_e + R_b \tag{6}$$

R_m was determined from the area specific resistance (ASR) data of Nafion$^{\circledR}$ 212 [56] and R_b from the conductivity provided in graphite plate data sheet (TF6 fluor polymer bipolar plate by SGL Carbon, Germany) [57]. The calculation of the carbon felt resistance R_e took into account the electronic conduction in the solid phase (i.e. the porous felts) and the ionic conduction in the liquid phase (i.e. the electrolytes). For the sake of simplicity, the Bruggeman correlation was used to evaluate the effective conductivity σ_f^{eff} of the porous felts [58]:

$$\sigma_f^{eff} = \sigma_s(1-\varepsilon)^{1.5} \tag{7}$$

where σ_s is the conductivity of the solid material constituting the felts and ε is their porosity after compression [59]:

$$\varepsilon = \frac{\varepsilon_0 - c_r}{1 - c_r} \tag{8}$$

In eq. (8), ε_0 is the porosity before compression and c_r is the felt compression ratio defined as:

$$c_r = 1 - \frac{h_{cr}}{h_0} \tag{9}$$

where h_0 and h_{cr} are the average electrode thickness before and after compression, respectively. By again taking into account the Bruggeman correlation, the effective electrolyte conductivity σ_{el}^{eff} at the positive and negative compartments was evaluated as:

$$\sigma_{el}^{eff} = \frac{F^2}{KT} \sum_j c_j z_j^2 \sigma_j \varepsilon^{1.5} \tag{10}$$

where K is the gas constant, T is the temperature, z is the number of electrons transferred in the reaction, c is the concentration and σ the conductivity of the reacting species; the subscript j stands for the species $V(IV)$, $V(V)$ in the positive electrode and for $V(II)$, $V(III)$ in the negative electrode. Given the state of charge of the positive and negative electrolytes SOC_+ and SOC_- and their total concentrations $c_+ = c_- = c_V$, each species concentration is given by:

$$c_{II} = c_- SOC_- \qquad\qquad c_{III} = c_-(1 - SOC_-) \tag{11}$$

$$c_{IV} = c_+(1 - SOC_+) \qquad\qquad c_V = c_+ SOC_+ \tag{12}$$

10

Table 1: Stack components physical properties

Component	Property	Value	Reference
Nafion® 212 membrane	Membrane area resistance (ASR) [Ω cm^2]	0.41	[56]
Beijing Great Wall, carbon felt electrode	Solid electrode conductivity σ_s [S m^{-1}]	1000	[58]
/	Felt porosity before compression ε_0	0.94	[60]
/	Felt thickness before compression h_0 [mm]	8.1	/
/	Felt thickness after compression h_{cr} [mm]	5.7	/
/	Felt compression ratio	0.3	/
TF6 fluor polymer bipolar plate by SGL Carbon	Bipolar plate resistivity σ_b [Ω cm]	7.6×10^{-4}	[57]
Liquid electrolyte	$V(II)$ conductivity σ_{II} [S m^{-1}]	27.5	[40]
/	$V(III)$ conductivity σ_{III} [S m^{-1}]	17.5	[40]
/	$V(IV)$ conductivity σ_{IV} [S m^{-1}]	27.7	[40]
/	$V(V)$ conductivity σ_V [S m^{-1}]	41.3	[40]

The resistances R_e of the porous electrodes soaked with liquid electrolytes were obtained as the parallel resistances of the two phases, for each cell compartment:

$$R_e = \left(\frac{1}{\sigma_f^{eff} + \sigma_{el+}^{eff}} + \frac{1}{\sigma_f^{eff} + \sigma_{el-}^{eff}} \right) \frac{N h_{cr}}{A} \qquad (13)$$

The parameters used in these calculations are listed in Tab.1. The measured and computed values of R_o present an acceptable agreement for the aim of this analysis. The results show that the electrodes provide the major contribution to the ohmic resistance, being R_e at least 70 % of R_o. The membrane resistance R_m contributes for about 20% and the graphite bipolar plate resistance R_b only for 10%. This evidence is in agreement with the results reported by Ke et. al. [16], indicating that in the flow-through distribution the contribution of the electrodes to the ohmic resistance is much higher than in other distributions, such as flow-by. In addition, the dependence of R_e on the SOC, expressed in eqs. 10, 11, 12 and 13 explains the behavior of R_o shown in Fig. 4.

3.3. Comparison of the loss equivalent resistances

The minimum internal electrical resistance $R_k(SOC) = -\Delta V_k / \Delta I$ involves that, at a given SOC, R_k presents the same linear behavior of $V(I)$ for any Q with $\alpha \geq \alpha_k$. In this condition, the electric power delivered by the battery at a

given SOC can be expressed as $P = V_0 I - R_k I^2$ with a constant $R_k \approx R_o$. To characterize the activation and transport losses in any conditions with $\alpha \leq \alpha_k$, eqs.(1), (2) and (5) can be combined to obtain:

$$\Delta V = R_i \, I = (R_k + R_t + R_a) \, I \qquad (14)$$

As far as $R_k(SOC)$ is known, by measuring $R_i = \Delta V/I$ at different SOC and Q, and thus at different α, from eq. (14) we obtain:

$$R_a + R_t = R_i - R_k \qquad (15)$$

Because $R_k = -\Delta V_k/\Delta I$ expresses the local slope of the polarization curve at $\alpha \geq \alpha_k$ starting from a current value $I > 0$ (i.e. in the full linearity ohmic region) and R_i expresses the mean slope of the polarization curve starting from $I = 0$, eq. (15) and also the relative difference $\Delta r = (R_i - R_k)/R_k$ constitutes an index of the incidence of $R_a + R_t$ and also of the non-linearity of the polarization curves. The plot of Fig. 5 also confirms that transport losses are the leading effect at small α: in these conditions R_t increases as α reduces and it can become even one order of magnitude larger than R_k. Furthermore, when both I and Q are small and $\alpha \to \alpha_k$ transport losses are small (i.e. R_t vanishes) and activation losses (i.e. R_a) become not negligible. It must be remarked at this point that once α reaches α_k, ensuring that the dominating resistance is R_o, increasing the flow rate only results in an increase of the hydraulic losses with no beneficial effect on the power conversion.

Instead, once the optimal flow regime is achieved (i.e. the battery operation is optimized) a further reduction of the internal losses (i.e. of R_k) can be obtained from an improved cell design. Consequently, tortuous porous microstructure of the electrodes, if properly designed, can promote a more efficient macroscopic diffusion of the species flowing through the electrodes: the faster the electrolyte mixes in the electrode pores, the higher the reaction rate. Recent studies of Maggiolo et al. [61] and Dentz et al. [62] indicate that this process involves an anomalous diffusivity, namely that the diffusion process presents a non-linear dependence on time. This means that the mean squared displacement (MSD) of the fluid particles varies more that linearly with time, whereas in a classical diffusion process this increase is linear [63]. However, to ensure an easy calculation, an effective diffusivity coefficient in the porous electrode can be used that, for liquids, is proportional to the average flow velocity (i.e. to Q), as usually done when the Bruggeman correlation is adopted [64].

The performance of a VRFB also depends on temperature: our tests were performed at a room temperature of 20 °C and the losses heat was removed by natural convection at piping and tanks. Temperature measurements picked up by the stack inlet and outlet sensors showed that the solution over temperatures during charge and discharge operations remained in the order of few degrees. More extended investigations on the correlation between battery performance and temperature are out of the scope of this paper and are reported elsewhere by means of a validated dynamical model which is generally described in [65], with a focus on high-current operations [66] and stand-by conditions [67].

4. Identifying optimal flow rate modulation

It is worth noticing that the global optimization of the flow rates, capable of minimizing the device losses and maximizing its efficiency, have to take into account all the flow-rate-related losses, which leads to modulate the flow rate according to the operating conditions. These Q-dependent losses consists of the internal losses due to cell overpotentials, which we have previously expressed as $P_i = R_i I^2$, together with the total losses P_w in the hydraulic circuits and their ancillaries, which occur in the stack, in the piping connecting stack and tanks, in the pumps, in the driving motors and in the controlling inverters. In IS-VRFB, P_w is measured by a specific wattmeter interposed between grid and inverters [68]:

$$P_Q = P_i + P_w \tag{16}$$

On the one hand, P_Q also depends on the stack current I and on the SOC; while on the other hand, the battery electric performance is also affected by the losses due to species crossover through the membranes, shunt currents and the losses in the power management system PMS. However, these losses do not vary with Q, so that they were not taken into account in the optimization of the flow rate.

Fig. 6 shows the profiles of P_Q as functions of the flow rate Q at different I and SOC values and Tab. 2 presents the combination of Q, SOC and I values used to build such profiles. The profiles highlight that every curve presents a minimum that identifies the electrolyte flow rate Q capable of minimizing P_Q for every SOC and I couple. Dynamically imposing these optimal Q results in the modulation of α, instead of a constant α: this modulated flow factor α_{opt} assures optimal operation, i.e. minimal losses and maximum efficiency. The results in Fig. 6 regard discharge operations, but similar considerations hold in the case of charge.

5. Implementation and validation

5.1. Implementing the control algorithm

The optimal control was made at a software level, by developing an apposite LabVIEW algorithm in the BMS of IS-VRFB. This algorithm uses the experimental data illustrated in Fig. 6 and Fig. 2, which were arranged in a 3-D matrix, as functions of Q, SOC and I values. The algorithm uses the matrix as a look-up table to identify the optimal Q_{opt} that minimizes P_Q for each couple of SOC and I operating values. Q_{opt} is then compared with the actual Q measured by the flowmeters and error signals are created which feed back the pump inverters with PID control routines. Consequently, the actual Q, and hence the actual α, is continuously modulated to match the minimum P_Q during the whole battery operation.

Table 2: Experimental campaign for optimal flow rate identification

SOC [%]	Applied current I [A]	Flow factor α [-]
20	10	4, 6, 8, 10, 12, 14, 16, 18, 20
20	30	4, 6, 8, 10, 12
40	10	6, 8, 10, 12, 14, 16, 18, 20
40	30	4, 6, 8, 10, 12, 14, 16, 18, 20
40	50	4, 6, 8, 10, 12, 14
40	70	6, 8, 10
60	10	8, 10, 12, 14, 16, 18, 20
60	30	4, 6, 8, 10, 12, 14, 16, 18, 20
60	50	4, 6, 8, 10, 12, 14, 16, 18, 20
60	70	4, 6, 8, 10, 12, 14, 16
80	10	12, 14, 16, 18, 20
80	30	6, 8, 10, 12, 14, 16, 18, 20
80	50	4, 6, 8, 10, 12, 14, 16, 18, 20
80	70	4, 6, 8, 10, 12, 14, 16, 18, 20

Table 3: Round trip efficiency (RTE) at different SOC range and current I at fixed α and modulated α_{opt}.

I [A]	SOC range [%]	RTE [%] fixed α	RTE [%] modulated α_{opt}
30	$13.1 - 87.0$	70.35	72.41
50	$19.9 - 78.5$	67.10	69.05
70	$28.0 - 72.7$	62.42	63.95

5.2. Validation tests

An experimental analysis of the effectiveness of the proposed optimal control of the electrolyte flow rate was performed [68]. These validation tests were carried out on IS-VRFB in charge/discharge cycles and the round-trip efficiency (RTE) was considered as the performance figure (the cost function of the optimization procedure). Consistent with the scope of this investigation, a definition of RTE was assumed that includes all Q-related losses P_Q [69]:

$$RTE = \frac{\int_{t_{dh}}[P(t) - P_w(t)]dt}{\int_{t_{ch}}[P(t) + P_w(t)]dt} \tag{17}$$

where $P(t) = V(t)I(t)$ is the electric power converted (consumed/delivered) by the stack. The results of the charge and discharge tests were compared with similar tests performed at constant α. In particular, a benchmark α was adopted, in accordance with the optimal $\alpha = 7.5$ reported in the literature [37]. Comparative tests showed that there was an RTE increase of around 2% when operating the VRFB at modulated α_{opt} with respect to the operation at constant α, as shown in Tab.3.

6. Conclusions

The experimental study that we performed on the 9 kW / 27 kWh IS-VRFB test facility has shown the effectiveness of modulating the electrolyte flow rate and flow factor to minimize the stack transport losses without affecting the electrical performance of a redox flow battery during charge and discharge cycles. This maximization of the efficiency requires control of the electrolyte flow rates so as to minimize the flow-rate depended losses under the constraint of providing a key flow factor to properly sustain the stack current at every electrolyte state of charge (i.e. with minimized transport losses). We have found that operating the battery at a modulated α_{opt} allows us to minimize the cell internal losses, which leads to an increase of the round trip efficiency of around 2% with respect to an operation at optimal constant flow factor (i.e. at $\alpha = 7.5$ as proposed in previous reports [37]).

Notably, the proposed flow factor modulation can be implemented at a software level in the control routines of the battery management system, without modifying the system hardware. This procedure required a preliminary experimental campaign that consists in mapping the flow factor values at different Q.

It is worth noting that the procedure presented here has a wide applicability and can be adopted in other RFBs, made with different materials for membranes and porous electrodes and even based on other chemistries.

In addition, two directions for future development emerge from the present study. On the one hand, the ohmic resistance results the leading parameter at optimized flow rate: reducing it will allow us to achieve larger limiting currents and higher deliverable powers. This target can be achieved by focusing on the electrode resistance that can constitute the major contribution to the total ohmic resistance, particularly in the case of flow-through architecture as in IS-VRFB. On the other hand, a reduction of the value of α_k and of the consequent pumping power can be achieved by using specifically designed porous electrodes with a microstructure that is capable of enhancing electrolyte dispersion to minimize the transport losses [60].

References

[1] G. Kear, A. A. Shah, F. C. Walsh, Development of the all-vanadium redox flow battery for energy storage: a review of technological, financial and policy aspects, International journal of energy research 36 (11) (2012) 1105–1120.

[2] S. Weber, J. F. Peters, M. Baumann, M. Weil, Life cycle assessment of a vanadium redox flow battery, Environmental science & technology 52 (18) (2018) 10864–10873.

[3] Z. Wei, S. Meng, K. J. Tseng, T. M. Lim, B. H. Soong, M. Skyllas-Kazacos, An adaptive model for vanadium redox flow battery and its application for online peak power estimation, Journal of Power Sources 344 (2017) 195–207.

[4] A. Khazaeli, A. Vatani, N. Tahouni, M. H. Panjeshahi, Numerical investigation and thermodynamic analysis of the effect of electrolyte flow rate on performance of all vanadium redox flow batteries, Journal of Power Sources 293 (2015) 599–612.

[5] C. Choi, S. Kim, R. Kim, Y. Choi, S. Kim, H.-y. Jung, J. H. Yang, H.-T. Kim, A review of vanadium electrolytes for vanadium redox flow batteries, Renewable and Sustainable Energy Reviews 69 (2017) 263–274.

[6] S. Roe, C. Menictas, M. Skyllas-Kazacos, A high energy density vanadium redox flow battery with 3 m vanadium electrolyte, Journal of The Electrochemical Society 163 (1) (2016) A5023–A5028.

[7] A. Di Blasi, N. Briguglio, O. Di Blasi, V. Antonucci, Charge–discharge performance of carbon fiber-based electrodes in single cell and short stack for vanadium redox flow battery, Applied Energy 125 (2014) 114–122.

[8] S. Kumar, S. Jayanti, Effect of flow field on the performance of an all-vanadium redox flow battery, Journal of Power Sources 307 (2016) 782–787.

[9] K. V. Greco, A. Forner-Cuenca, A. Mularczyk, J. Eller, F. R. Brushett, Elucidating the nuanced effects of thermal pretreatment on carbon paper electrodes for vanadium redox flow batteries, ACS applied materials & interfaces 10 (51) (2018) 44430–44442.

[10] R. Banerjee, N. Bevilacqua, L. Eifert, R. Zeis, Characterization of carbon felt electrodes for vanadium redox flow batteries–a pore network modeling approach, Journal of Energy Storage 21 (2019) 163–171.

[11] C. Sun, A. Zlotorowicz, G. Nawn, E. Negro, F. Bertasi, G. Pagot, K. Vezzù, G. Pace, M. Guarnieri, V. Di Noto, [nafion/(wo3) x] hybrid membranes for vanadium redox flow batteries, Solid State Ionics 319 (2018) 110–116.

[12] Y. Lei, B. Zhang, Z. H. Zhang, B. F. Bai, T. Zhao, An improved model of ion selective adsorption in membrane and its application in vanadium redox flow batteries, Applied Energy 215 (2018) 591–601.

[13] Y. Ashraf Gandomi, D. Aaron, M. Mench, Influence of membrane equivalent weight and reinforcement on ionic species crossover in all-vanadium redox flow batteries, Membranes 7 (2) (2017) 29.

[14] R. Badrinarayanan, J. Zhao, K. Tseng, M. Skyllas-Kazacos, Extended dynamic model for ion diffusion in all-vanadium redox flow battery including the effects of temperature and bulk electrolyte transfer, Journal of Power Sources 270 (2014) 576–586.

[15] R. M. Darling, M. L. Perry, The influence of electrode and channel configurations on flow battery performance, Journal of The Electrochemical Society 161 (9) (2014) A1381–A1387.

[16] X. Ke, J. M. Prahl, J. I. D. Alexander, J. S. Wainright, T. A. Zawodzinski, R. F. Savinell, Rechargeable redox flow batteries: flow fields, stacks and design considerations, Chemical Society Reviews 47 (23) (2018) 8721–8743.

[17] Q. Zheng, F. Xing, X. Li, G. Ning, H. Zhang, Flow field design and optimization based on the mass transport polarization regulation in a flow-through type vanadium flow battery, Journal of Power Sources 324 (2016) 402–411.

[18] L. F. Arenas, C. P. de León, F. C. Walsh, Redox flow batteries for energy storage: their promise, achievements and challenges, Current Opinion in Electrochemistry.

[19] L. Arenas, C. P. De León, F. Walsh, Engineering aspects of the design, construction and performance of modular redox flow batteries for energy storage, Journal of Energy Storage 11 (2017) 119–153.

[20] Q. Xu, T. Zhao, P. Leung, Numerical investigations of flow field designs for vanadium redox flow batteries, Applied energy 105 (2013) 47–56.

[21] M. J. Watt-Smith, P. Ridley, R. Wills, A. Shah, F. Walsh, The importance of key operational variables and electrolyte monitoring to the performance of an all vanadium redox flow battery, Journal of Chemical Technology & Biotechnology 88 (1) (2013) 126–138.

[22] M. Pugach, M. Kondratenko, S. Briola, A. Bischi, Zero dimensional dynamic model of vanadium redox flow battery cell incorporating all modes of vanadium ions crossover, Applied energy 226 (2018) 560–569.

[23] Y. Li, X. Zhang, J. Bao, M. Skyllas-Kazacos, Studies on optimal charging conditions for vanadium redox flow batteries, Journal of Energy Storage 11 (2017) 191–199.

[24] H. Al-Fetlawi, A. Shah, F. Walsh, Modelling the effects of oxygen evolution in the all-vanadium redox flow battery, Electrochimica Acta 55 (9) (2010) 3192–3205.

[25] M. Guarnieri, P. Mattavelli, G. Petrone, G. Spagnuolo, Vanadium redox flow batteries: potentials and challenges of an emerging storage technology, IEEE Industrial Electronics Magazine 10 (4) (2016) 20–31.

[26] M. Guarnieri, A. Bovo, A. Giovannelli, P. Mattavelli, A real multitechnology microgrid in venice: A design review, IEEE Industrial Electronics Magazine 12 (3) (2018) 19–31.

[27] Z. Wei, J. Zhao, B. Xiong, Dynamic electro-thermal modeling of all-vanadium redox flow battery with forced cooling strategies, Applied energy 135 (2014) 1–10.

[28] R. Badrinarayanan, K. J. Tseng, B. H. Soong, Z. Wei, Modelling and control of vanadium redox flow battery for profile based charging applications, Energy 141 (2017) 1479–1488.

[29] Y. Li, X. Zhang, J. Bao, M. Skyllas-Kazacos, Control of electrolyte flow rate for the vanadium redox flow battery by gain scheduling, Journal of Energy Storage 14 (2017) 125–133.

[30] S. Rudolph, U. Schröder, R. Bayanov, K. Blenke, I. Bayanov, Optimal electrolyte flow distribution in hydrodynamic circuit of vanadium redox flow battery, Journal of Electroanalytical Chemistry 736 (2015) 117–126.

[31] W. Yang, F. Yan, Z. Qu, Y. He, Effect of various strategies of soc-dependent operating current on performance of a vanadium redox flow battery, Electrochimica Acta 259 (2018) 772–782.

[32] Q. Xu, T. Zhao, C. Zhang, Effects of soc-dependent electrolyte viscosity on performance of vanadium redox flow batteries, Applied Energy 130 (2014) 139–147.

[33] C. Ling, H. Cao, M. Chng, M. Han, E. Birgersson, Pulsating electrolyte flow in a full vanadium redox battery, Journal of Power Sources 294 (2015) 305–311.

[34] X. Ma, H. Zhang, C. Sun, Y. Zou, T. Zhang, An optimal strategy of electrolyte flow rate for vanadium redox flow battery, Journal of power sources 203 (2012) 153–158.

[35] J. Fu, T. Wang, X. Wang, J. Sun, M. Zheng, Dynamic flow rate control for vanadium redox flow batteries, Energy Procedia 105 (2017) 4482–4491.

[36] W. Xiao, L. Tan, Control strategy optimization of electrolyte flow rate for all vanadium redox flow battery with consideration of pump, Renewable Energy.

[37] A. Tang, J. Bao, M. Skyllas-Kazacos, Studies on pressure losses and flow rate optimization in vanadium redox flow battery, Journal of power sources 248 (2014) 154–162.

[38] S. König, M. Suriyah, T. Leibfried, Innovative model-based flow rate optimization for vanadium redox flow batteries, Journal of Power Sources 333 (2016) 134–144.

[39] M. Guarnieri, A. Trovò, A. D'Anzi, P. Alotto, Developing vanadium redox flow technology on a 9-kw 26-kwh industrial scale test facility: Design review and early experiments, Applied Energy 230 (2018) 1425–1434.

[40] F. Moro, A. Trovò, S. Bortolin, D. Del Col, M. Guarnieri, An alternative low-loss stack topology for vanadium redox flow battery: Comparative assessment, Journal of Power Sources 340 (2017) 229–241.

[41] M. Guarnieri, A. Trovò, G. Marini, A. Sutto, P. Alotto, High current polarization tests on a 9 kw vanadium redox flow battery, Journal of Power Sources 431 (2019) 239–249.

[42] Z. Wei, A. Bhattarai, C. Zou, S. Meng, T. M. Lim, M. Skyllas-Kazacos, Real-time monitoring of capacity loss for vanadium redox flow battery, Journal of Power Sources 390 (2018) 261–269.

[43] Z. Wei, K. J. Tseng, N. Wai, T. M. Lim, M. Skyllas-Kazacos, Adaptive estimation of state of charge and capacity with online identified battery model for vanadium redox flow battery, Journal of Power Sources 332 (2016) 389–398.

[44] C. Sun, J. Chen, H. Zhang, X. Han, Q. Luo, Investigations on transfer of water and vanadium ions across nafion membrane in an operating vanadium redox flow battery, Journal of Power Sources 195 (3) (2010) 890–897.

[45] Y. A. Gandomi, D. Aaron, J. Houser, M. Daugherty, J. Clement, A. Pezeshki, T. Ertugrul, D. Moseley, M. Mench, Critical review—experimental diagnostics and material characterization techniques used on redox flow batteries, Journal of The Electrochemical Society 165 (5) (2018) A970–A1010.

[46] J. Fu, M. Zheng, X. Wang, J. Sun, T. Wang, Flow-rate optimization and economic analysis of vanadium redox flow batteries in a load-shifting application, Journal of Energy Engineering 143 (6) (2017) 04017064.

[47] L. J. Ontiveros, P. E. Mercado, Modeling of a vanadium redox flow battery for power system dynamic studies, International Journal of Hydrogen Energy 39 (16) (2014) 8720–8727.

[48] Y. Li, J. Bao, M. Skyllas-Kazacos, M. P. Akter, X. Zhang, J. Fletcher, Studies on dynamic responses and impedance of the vanadium redox flow battery, Applied Energy 237 (2019) 91–102.

[49] J.-Y. Chen, C.-L. Hsieh, N.-Y. Hsu, Y.-S. Chou, Y.-S. Chen, Determining the limiting current density of vanadium redox flow batteries, Energies 7 (9) (2014) 5863–5873.

[50] S. Ressel, A. Laube, S. Fischer, A. Chica, T. Flower, T. Struckmann, Performance of a vanadium redox flow battery with tubular cell design, Journal of Power Sources 355 (2017) 199–205.

[51] M. Pugach, V. Vyshinsky, A. Bischi, Energy efficiency analysis for a kilowatt class vanadium redox flow battery system, Applied Energy 253 (2019) 113533.

[52] T. Wang, J. Fu, M. Zheng, Z. Yu, Dynamic control strategy for the electrolyte flow rate of vanadium redox flow batteries, Applied Energy 227 (2018) 613–623.

[53] B. Xiong, J. Zhao, K. J. Tseng, M. Skyllas-Kazacos, T. M. Lim, Y. Zhang, Thermal hydraulic behavior and efficiency analysis of an all-vanadium redox flow battery, Journal of Power Sources 242 (2013) 314–324.

[54] S. Kim, E. Thomsen, G. Xia, Z. Nie, J. Bao, K. Recknagle, W. Wang, V. Viswanathan, Q. Luo, X. Wei, et al., 1 kw/1 kwh advanced vanadium redox flow battery utilizing mixed acid electrolytes, Journal of Power Sources 237 (2013) 300–309.

[55] D.-J. Park, K.-S. Jeon, C.-H. Ryu, G.-J. Hwang, Performance of the all-vanadium redox flow battery stack, Journal of Industrial and Engineering Chemistry 45 (2017) 387–390.

[56] X. Yan, J. Sun, L. Gao, W. Zheng, Y. Dai, X. Ruan, G. He, A novel long-side-chain sulfonated poly (2, 6-dimethyl-1, 4-phenylene oxide) membrane for vanadium redox flow battery, International Journal of Hydrogen Energy 43 (1) (2018) 301–310.

[57] Sgl carbon.
URL https://www.sglcarbon.com/en/markets-solutions/material/sigracell-bipolar-plates-and-end-plates/

[58] X. Ma, H. Zhang, F. Xing, A three-dimensional model for negative half cell of the vanadium redox flow battery, Electrochimica Acta 58 (2011) 238–246.

[59] Q. Wang, Z. Qu, Z. Jiang, W. Yang, Experimental study on the performance of a vanadium redox flow battery with non-uniformly compressed carbon felt electrode, Applied Energy 213 (2018) 293–305.

[60] D. Maggiolo, F. Zanini, F. Picano, A. Trovò, S. Carmignato, M. Guarnieri, Particle based method and x-ray computed tomography for pore-scale flow characterization in vrfb electrodes, Energy Storage Materials 16 (2019) 91–96.

[61] D. Maggiolo, F. Picano, M. Guarnieri, Flow and dispersion in anisotropic porous media: A lattice-boltzmann study, Physics of Fluids 28 (10) (2016) 102001.

[62] M. Dentz, M. Icardi, J. J. Hidalgo, Mechanisms of dispersion in a porous medium, Journal of Fluid Mechanics 841 (2018) 851–882.

[63] J.-P. Bouchaud, A. Georges, Anomalous diffusion in disordered media: statistical mechanisms, models and physical applications, Physics reports 195 (4-5) (1990) 127–293.

[64] B. Tjaden, S. J. Cooper, D. J. Brett, D. Kramer, P. R. Shearing, On the origin and application of the bruggeman correlation for analysing transport phenomena in electrochemical systems, Current Opinion in Chemical Engineering 12 (2016) 44–51.

[65] A. Trovò, P. Alotto, M. Giomo, F. Moro, M. Guarnieri, A validated dynamical model of a kw-class vanadium redox flow battery, Mathematics and Computers in Simulationdoi:https://doi.org/10.1016/j.matcom.2019.12.011.

[66] A. Trovò, A. Saccardo, M. Giomo, M. Guarnieri, Thermal modeling of industrial-scale vanadium redox flow batteries in highcurrent operations, Journal of power sources 424 (2019) 204–214.

[67] A. Trovò, G. Marini, A. Sutto, P. Alotto, M. Giomo, F. Moro, M. Guarnieri, Standby thermal model of a vanadium redox flow battery stack with crossover and shunt-current effects, Applied Energy 240 (2019) 893–906.

[68] A. Trovò, F. Picano, M. Guarnieri, Comparison of energy losses in a 9 kw vanadium redox flow battery, Journal of Power Sources 440 (2019) 227144.

[69] A. Trovò, F. Picano, M. Guarnieri, Maximizing vanadium redox flow battery efficiency: Strategies of flow rate control, in: 2019 IEEE 28th International Symposium on Industrial Electronics (ISIE), IEEE, 2019, pp. 1977–1982.
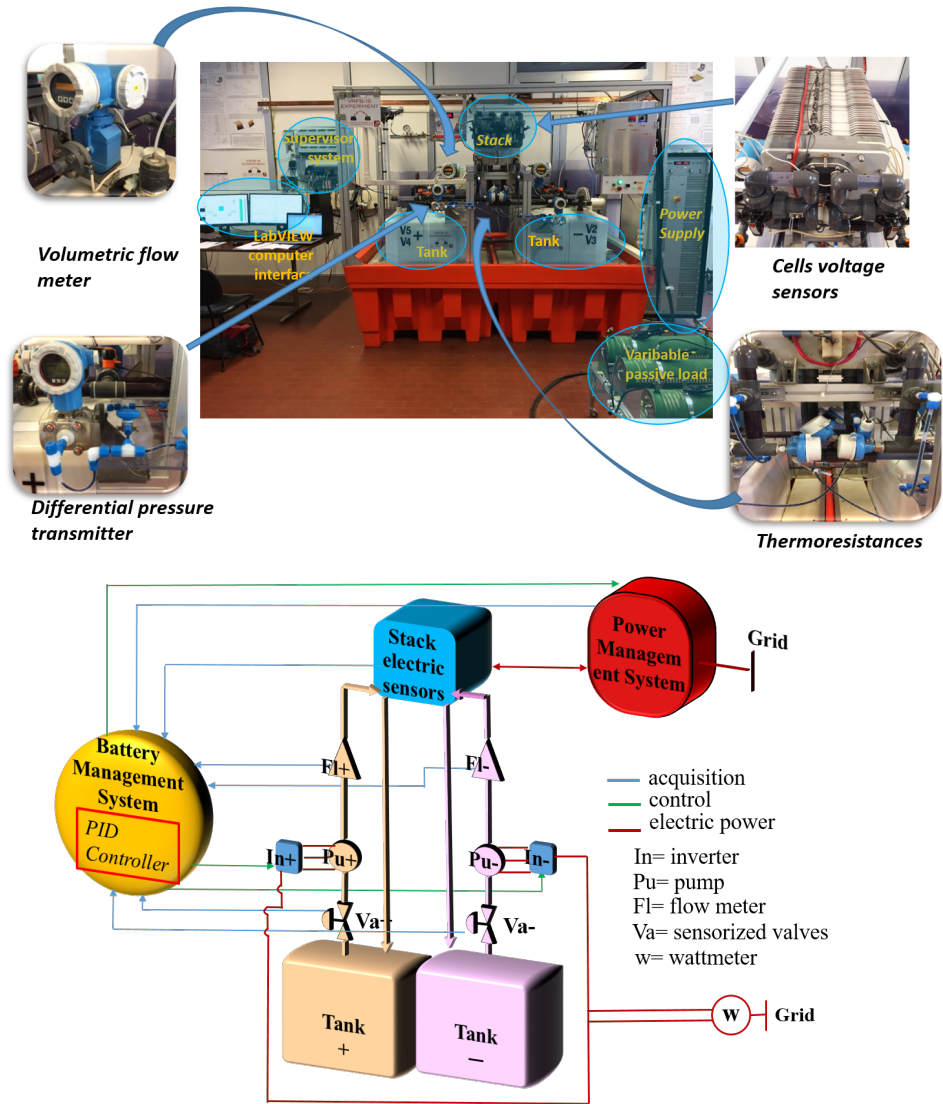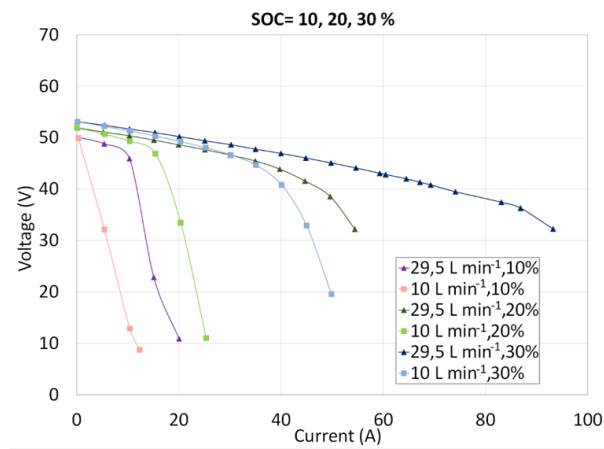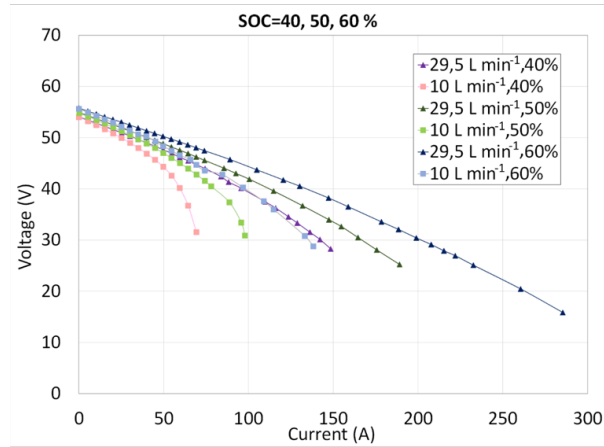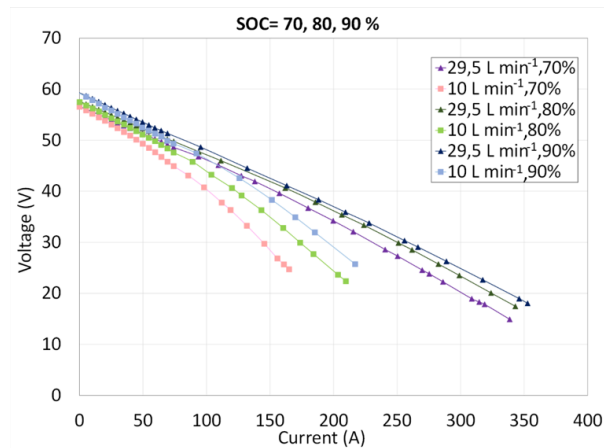
Figure 1: The 9 kW/27 kWh IS-VRFB test facility with its subsystems and scheme of the facility control system. The industrial-scale laboratory VRFB was used in the experimental campaigns which provided the data upon which the study was developed.
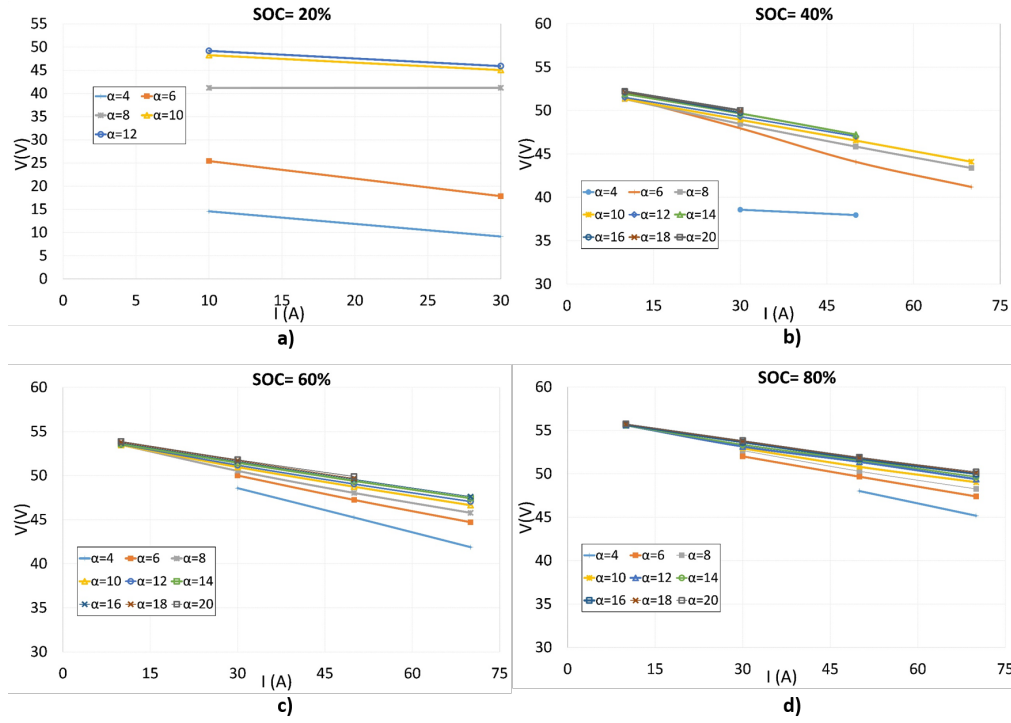
Figure 2: Experimental polarization curves (V vs. I) during discharge obtained on the IS-VRFB test facility at different flow rates: Q 23 10 L min^{-1} ($q = 6.910^{-3}$ cm s^{-1}) and 29.5 L min^{-1} ($q = 20.510^{-3}$ cm s^{-1}): a) $SOC = 10\%$, 20%, 30%; b) $SOC = 40\%$, 50%, 60%; c) $SOC = 70\%$, 80%, 90%.

Figure 3: Experimental polarization curves (V vs. I) during discharge obtained on the IS-VRFB test facility at fixed flow factors α at different SOC: a) $SOC = 20\%$, b) $SOC = 40\%$, c) $SOC = 60\%$, d) $SOC = 80\%$.
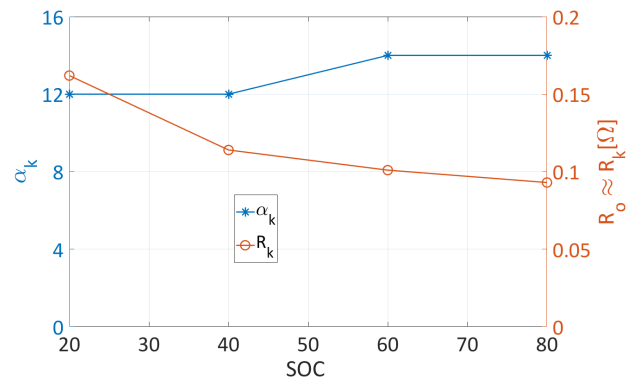

Figure 4: Key flow factor α_k and corresponding key electrical resistance $R_o \simeq R_k$ vs. SOC.
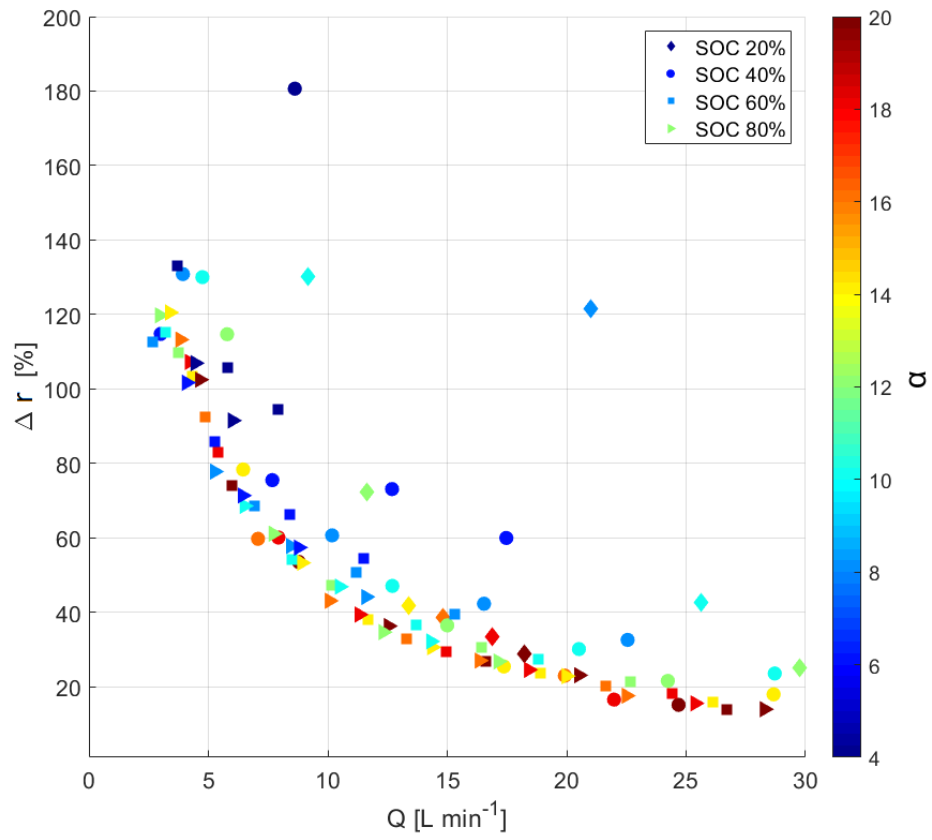
24

Figure 5: Relative difference between resistance R_i and R_k at different flow rate Q, different flow factor α and different SOC. Data point are code-colored as function of α, showing that as α increases this fraction Δr tends to a minimum value dependent on Q and independent of SOC.
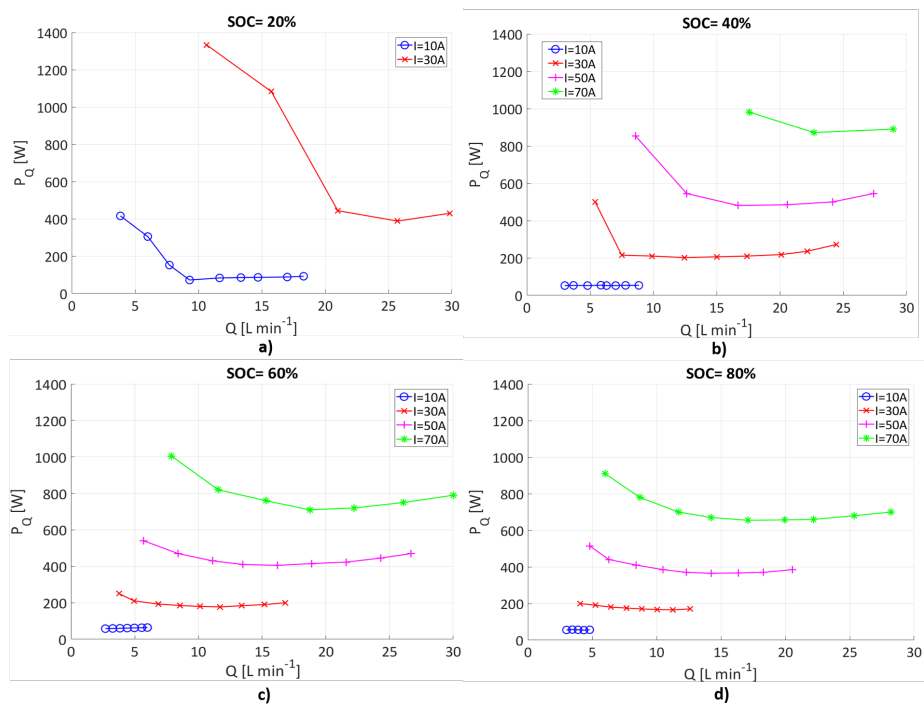
Figure 6: Flow-rate dependent losses P_Q by contours plotted for different current I and flow rate Q: a) $SOC = 20\%$, b) $SOC = 40\%$, c) $SOC = 60\%$, d) $SOC = 80\%$.

26